ACSNANO

www.acsnano.org

ARTICLE

Zigzag HgTe Nanowires Modify the Electron–Phonon Interaction in Chirality-Refined Single-Walled Carbon Nanotubes

Ziyi Hu,* Ben Breeze, Reza J. Kashtiban, Jeremy Sloan,* and James Lloyd-Hughes*

Cite This: *ACS Nano* 2022, 16, 6789–6800

Read Online

ACCESS | Metrics & More | Article Recommendations | Supporting Information

ABSTRACT: Atomically thin nanowires (NWs) can be synthesized inside single-walled carbon nanotubes (SWCNTs) and feature unique crystal structures. Here we show that HgTe nanowires formed inside small-diameter (<1 nm) SWCNTs can advantageously alter the optical and electronic properties of the SWCNTs. Metallic purification of the filled SWCNTs was achieved by a gel column chromatography method, leading to an efficient extraction of the semiconducting and metallic portions with known chiralities. Electron microscopic imaging revealed that zigzag HgTe chains were the dominant NW geometry in both the semiconducting and metallic species. Equilibrium-state and ultrafast spectroscopy demonstrated that the coupled electron–phonon system was modified by the encapsulated HgTe NWs, in a way that varied with the chirality. For semiconducting SWCNTs with HgTe NWs, Auger relaxation processes were suppressed, leading to enhanced photoluminescence emission. In contrast, HgTe NWs enhanced the Auger relaxation rate of metallic SWCNTs and created faster phonon relaxation, providing experimental evidence that encapsulated atomic chains can suppress hot carrier effects and therefore boost electronic transport.

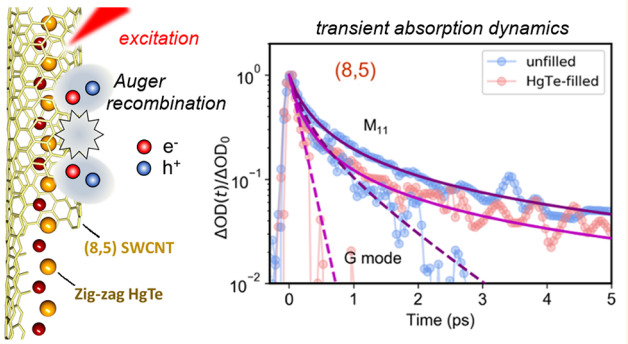

KEYWORDS: *single-walled carbon nanotubes, mercury telluride, ultrafast spectroscopy, exciton dynamics, Auger recombination*

Carbon nanotubes provide a facile and versatile template for the fabrication of quasi-1D heterostructures. Unique nanoscale materials and composites can be created by various means either internal to the nanotube—such as filling their central void[1]—or by external methods, which include wrapping by conjugated polymers,[2] selective doping,[3,4] and overgrowth with van der Waals heterostructures.[5,6] These methods provide opportunities to tailor the optical and electrical properties of single-walled carbon nanotubes (SWCNTs), as well as creating composites with distinct functionality and where charge or energy can flow between the constituents.[6,7]

Among these various approaches, filling the central pore of a SWCNT with a guest material offers the additional benefit of creating an unconventional 1D nanostructure that cannot be directly synthesized in free space. Previous experimental works have shown that various kinds of materials, including pure metals,[8,9] metal chalcogenides,[10−14] metal halides,[15−17] graphene nanoribbons,[18] C_{60},[1] water molecules,[19,20] white phosphorus,[21] iodine,[22] alkane molecules,[23] and dye molecules,[7] can successfully be encapsulated inside SWCNTs. When binary compounds crystallize inside narrow SWCNTs, the restricted volume leads to atomically thin nanowires (NWs) that adopt different structures, such as linear chains,[13,17] zigzag chains,[13] and helical chains,[17] depending on the SWCNT diameter.

The extent to which the NW modifies the electronic, excitonic, and vibrational states of the encapsulating SWCNT is of great potential interest as a way to tune the unique physical properties of SWCNTs. While the strong Coulomb interaction in a bare SWCNT leads to large exciton binding energies,[24] it also leads to rapid scattering processes that involve multiple charge carriers, such as Auger recombination (exciton–exciton annihilation),[25,26] and which limits the quantum efficiency of light emission.[27,28] Investigating whether NW encapsulation alters Auger recombination in SWCNTs is

Received: February 16, 2022
Accepted: April 4, 2022
Published: April 7, 2022

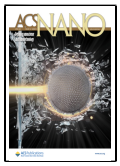

https://doi.org/10.1021/acsnano.2c01647
ACS Nano 2022, 16, 6789–6800

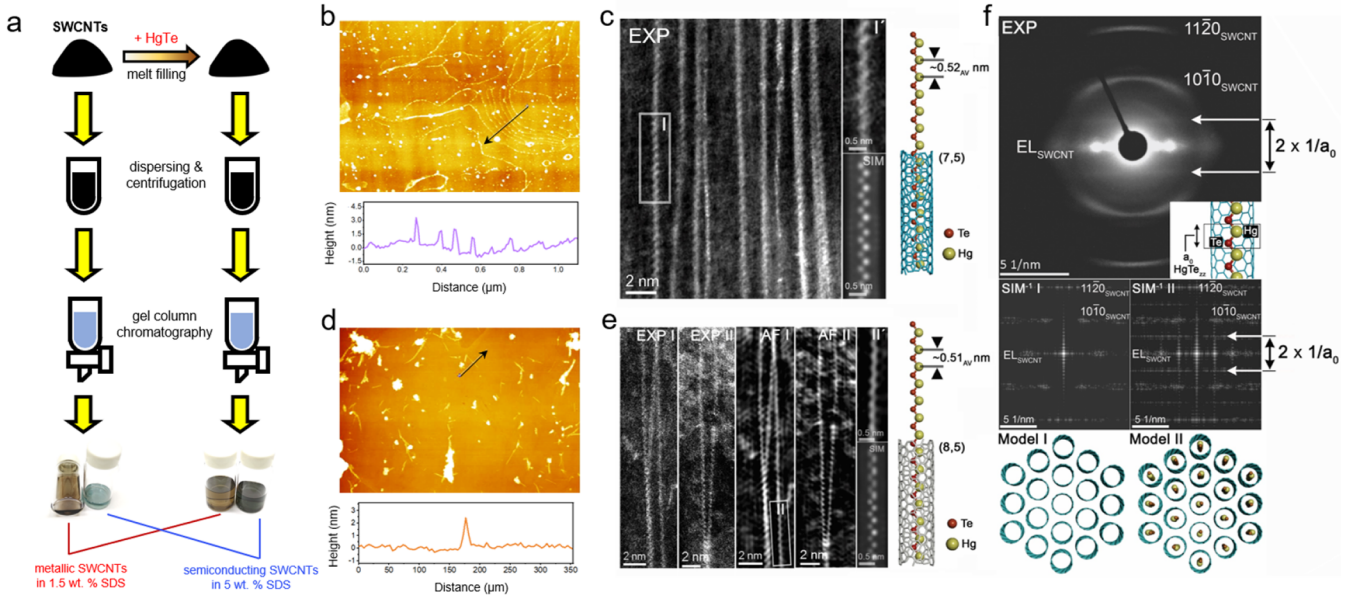

Figure 1. (a) Schematic of SWCNT filling and chirality sorting methodology. (b, d) AFM height and cross-section profiles of the (b) semiconducting and (d) metallic SWCNTs. Arrowed lines illustrate the positions and orientations of the profiles. The width of scanned areas were (b) 5 and (d) 2 μm. (c) ADF-STEM image showing an array of HgTe-filled SWCNTs encapsulated by zigzag chains observed in the semiconducting SWCNT sample. The adapted filtered detail I′ is enlarged from I, and the corresponding simulation ("SIM") is based on the model, right. (e) As for (c) but two representative regions (EXP I and EXP II). Adaptive filtered versions of these images are shown in AF I and AF II, respectively. A detail from AF I is shown in II and then simulated ("SIM" below) according to the model, right. (f) Experimental ED pattern (top) of a bundle of reagglomerated HgTe-filled semiconducting SWCNTs (inset is the microstructure) with repeating 1D unit cell (lattice parameter a_0). SIM^{-1} I and SIM^{-1} II are FFTs of multislice simulations of models I (unfilled SWCNT bundle) and II (zigzag HgTe-filled bundle), respectively, imaged orthogonally to these end-on projections.

therefore of substantial interest. Further, significant electron–phonon coupling can cause nonequilibrium electrons to heat the phonon population if the phonon decay rate is smaller than the electron–phonon scattering rate, as reported for a variety of materials including carbon nanotubes.[29−31] Electron–phonon coupling is particularly prominent in metallic SWCNT devices under strong electric fields, where electron scattering with a hot optical phonon population limits the tube's conductivity.[29,30] Computational models have predicted that phonon–phonon decay rates can be enhanced by encapsulating 1D atomic chains in metallic SWCNTs: the acoustic phonon modes of the encapsulated NWs provide additional routes by which the Γ- and K- point phonons can decay, thereby preventing long-lived phonons and ultimately increasing the current flow achievable along the CNT at high bias.[30]

In this Article we report direct experimental measurements of the influence of nanowire infiltration on electron–phonon coupling and phonon–phonon decay processes in SWCNTs. We focused on HgTe nanowires encapsulated inside narrow-diameter SWCNTs. The choice of SWCNT diameters below 1 nm conveniently allowed optical studies of the excitonic transitions of the CNTs in the technologically relevant UV, visible, and near-infrared ranges. We chose to investigate filling using HgTe NWs, as high filling fractions can be achieved *via* melt infiltration.[12] Previous work on HgTe NWs in wider SWCNTs (between 1.35 and 1.5 nm) demonstrated a tubular form composed of heavily distorted Hg_2Te_2 parallelogram bilayers linked by trigonal bonding[10] and which displayed sharp Raman vibrational features.[12] In this study, we report the synthesis of zigzag phase HgTe nanowires inside sub-1-nm-thick SWCNTs using melt infiltration, as confirmed by transmission electron microscopic imaging and diffraction. *Via* a detailed optical characterization, utilizing equilibrium-state fluorescence and Raman spectroscopy, and ultrafast transient absorption spectroscopy (TAS), we demonstrate experimentally that HgTe encapsulation produces substantial modifications to the electron–phonon coupling, phonon–phonon decay, and Auger recombination processes active in SWCNTs. Significantly, the impact of HgTe nanowire infiltration depended on the chirality of the encapsulating SWCNT.

RESULTS AND DISCUSSION

Structure and Morphology. A previous *ab initio* computational study predicted that the formation of zigzag-type SnTe atomic chains is energetically favored for SWCNTs with a size of 0.76–0.95 nm.[13] We therefore studied SWCNTs within this diameter range (*e.g.*, (7,5) 0.83 nm, (8,4) 0.84 nm, (10,2) 0.88 nm, (7,6) 0.90 nm, (9,4) 0.92 nm, and (8,6) 0.97 nm) that were filled with HgTe NWs *via* a melt infiltration process. Compared to other larger-diameter (*e.g.*, over 1 nm) SWCNTs, these sub-1-nm-thick SWCNTs possess larger bandgaps and hence show the advantage of providing discrete near-infrared absorption/photoluminescence features. Along with NW filling inside the SWCNTs, synthesis *via* melt infiltration can also lead to the nanoparticle growth on the outside of nanotubes and introduce guest atoms onto the sp^2 carbon lattice. Most research on filled SWCNTs thus far has studied nonpurified material or adopted methodologies that can only partially remove the impurities (*e.g.*, acid washing). Here we adopted a synthesis and refinement process that used ultracentrifugation and gel column chromatography after melt filling to yield semiconducting and metallic species, which

https://doi.org/10.1021/acsnano.2c01647
ACS Nano 2022, 16, 6789−6800

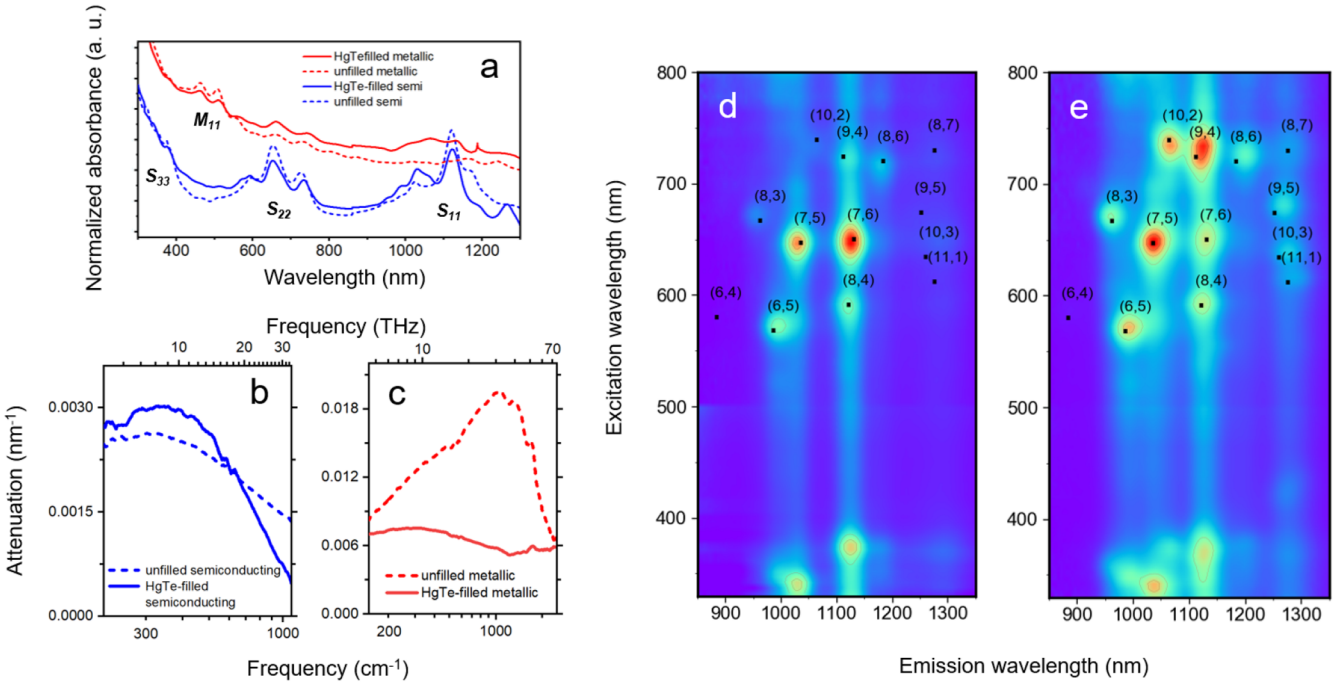

Figure 2. (a) UV−vis−NIR absorption of the unfilled and HgTe-filled SWCNT solutions. The spectra are normalized to the absorbance values at 400 nm, where there are no expected excitonic features. (b, c) Room-temperature infrared attenuation of the semiconducting and metallic SWCNT films divided by their thicknesses. (d, e) PLE maps of the solution-state (d) unfilled and (e) HgTe-filled semiconducting SWCNTs. Black dots show the S_{22} and S_{11} wavelengths for each (*n*,*m*) species according to the empirical model.[32]

presented a green and dark yellow color, respectively, as depicted in Figure 1(a). Annular dark-field scanning transmission electron microscopic (ADF-STEM) images found that a large quantity of nanoparticles coexisted with the SWCNTs after a mild purification treatment (centrifugation under a low force), whereas they were effectively removed under a sufficiently high centrifugal force (Figure S1).

The morphology of the refined, filled SWCNTs was uncovered by the atomic force microscopic (AFM) studies on specimens taken from dilute, dispersed solutions. The semiconducting SWCNT sample was found to consist of nanotubes a few microns long (Figure 1(b)), while the metallic SWCNT sample showed shorter lengths below 500 nm (Figure 1(c)). Besides nanotubes, nanoparticles can also be observed in the AFM images. According to peak force error maps of the same regions, a huge contrast between the nanotubes and nanoparticles was found (Figure S2), suggesting that these particles are likely to be soft organic compounds such as surfactant aggregates, rather than residual catalysts or HgTe nanocrystals.

The detailed atomic structure of HgTe NWs in the chirality-refined semiconducting and metallic SWCNTs was investigated by ADF-STEM (Figure 1(d) and (e)). For both types of samples, discrete zigzag HgTe chains were observed, with an average period of ∼0.52 nm for semiconducting SWCNTs and ∼0.51 nm for metallic SWCNTs, as shown in the representative inset models on the right-hand side of each panel. In Figure 1(f) an electron diffraction (ED) pattern obtained from an aligned bundle of reagglomerated semiconducting SWCNTs filled with zigzag HgTe chains is shown, which contains two extra diffraction features separated by a distance ($2 \times 1/a_0$), where a_0 is the period of a quasi 1D zigzag HgTe chain, as depicted in the model inset into the experimental ED pattern. As can be seen from the two ED simulations in the bottom insets (SIM^{-1} I and SIM^{-1} II), which correspond to the diffraction behavior of model I (empty SWCNTs) and model II (SWCNTs filled with randomly oriented zigzag HgTe chains), the extra diffraction feature arises from the 1D zigzag chains. The value for a_0 measured from the experimental diffraction pattern corresponds to ∼0.525 nm, consistent with measurements obtained from the real-space images in Figure 1(d) and (e) within experimental error. Analysis based on the energy-dispersive X-ray (EDX) spectrum yields a Hg:Te ratio of 1:1, further verifying the formation of HgTe (Figure S3).

Optical Absorbance: Excitons and Plasmons. We now discuss the optoelectronic properties of the HgTe/SWCNT heterostructures, as assessed by equilibrium-state optical spectroscopy on solutions (Figure 2) and thin films (Figure S4). Spectra were normalized at 400 nm in order to correct for variations in CNT concentration between different solutions. The ultraviolet−visible−near-infrared (UV−vis−NIR) absorbance spectra (Figure 2(a)) reveal several absorption lines corresponding to the different excitonic transitions of SWCNTs (*e.g.*, S_{11}, S_{22}, S_{33}, and M_{11}). For the semiconducting samples, two dominant absorption lines in the regions 645−650 nm and 1120−1130 nm were found, linked to the S_{22} and S_{11} transitions of (7,6), and are suggestive of a dominant (7,6) chirality. For the metallic SWCNT samples, two absorbance lines located at ∼460 and ∼507 nm are evident, which can be ascribed to the M_{11} excitonic transitions. For the thin films, a marked red-shift of the excitonic peaks can be observed in Figure S4 (*e.g.*, S_{22} and S_{11} bands red-shifted to ∼670 and ∼1190 nm and two M_{11} bands red-shifted to ∼468 and ∼510 nm), which can be attributed to strong rebundling when the nanotubes condensed into films.

To investigate the impact of HgTe filling on the conductivity of free carriers, mid- and far-infrared attenuation spectra of thin

https://doi.org/10.1021/acsnano.2c01647
ACS Nano 2022, 16, 6789−6800

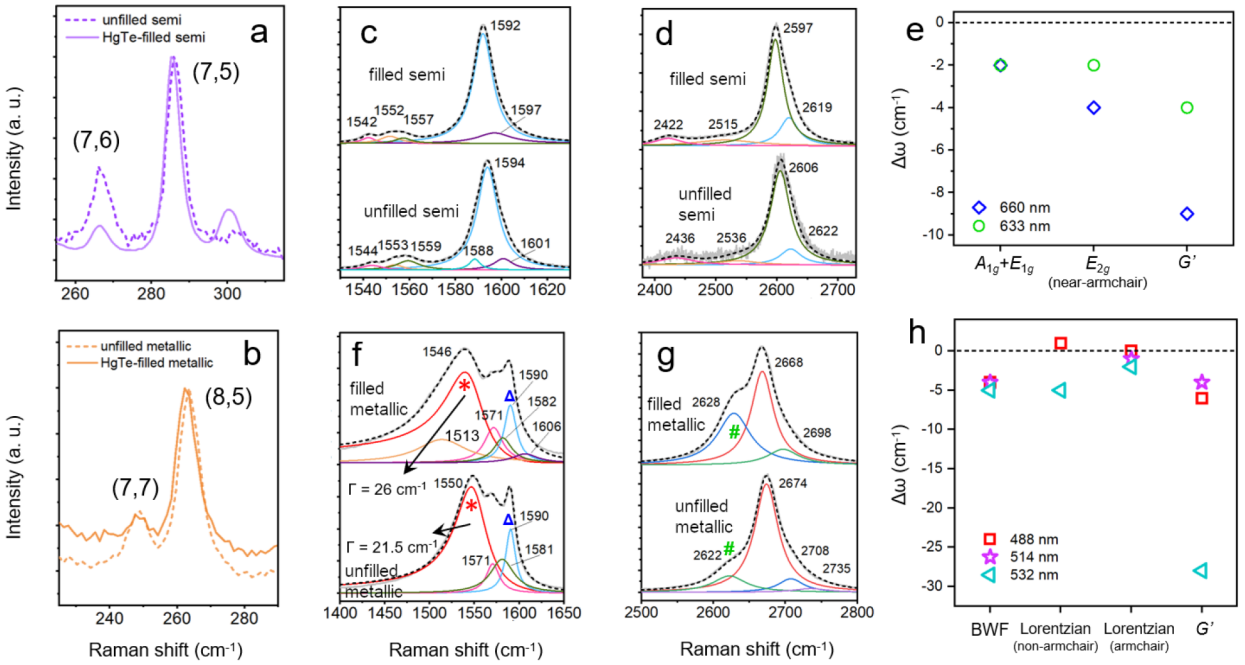

Figure 3. Raman spectra of the RBMs of (a) semiconducting SWCNTs (under 660 nm excitation) and the (b) metallic SWCNTs (488 nm excitation), with (solid lines) and without (dashed lines) HgTe filling. The (c) G and (d) G′ modes of the semiconducting samples are shown under 660 nm excitation, along with (e) the spectral shifts caused by HgTe filling for the strongest modes. The (f) G and (g) G′ modes of the metallic samples are reported under 514 nm excitation. The BWF line of non-armchair metallic species (red asterisks) and an additional Lorentzian component at 1590 cm^{-1} (blue triangles) are also shown. The green number sign marks a second component of the G′ mode of the metallic samples. (h) Spectral shifts created by filling the metallic samples.

films of materials produced by the vacuum filtration method were obtained, as reported in Figure 2(b) and (c). The broad absorption maxima in the free-carrier absorption regime (below 3000 cm^{-1}) result from the axial plasmon resonance of finite-length nanotubes.[4,33−35] The absorbance profiles for semiconducting and metallic SWCNTs are distinctly different. The semiconducting SWCNTs exhibited a narrower absorption peak centered at around 300 cm^{-1}, while the metallic tubes had a broader absorption peak around 1000 cm^{-1}. We note that the theory of axial plasmons in SWCNTs[33] predicts the plasmon resonance frequency to vary inversely with tube length, l, according to $\omega_0 = \pi v_q(l, d, N)/l$, where $v_q(l, d, N)$ is the plasmon mode velocity, a function of the tube diameter d = 0.88 nm and length and also of the number of nanotubes in each bundle.[33] The bundle dependence has not been previously considered in comparisons between the experimental plasmon frequency and theory.[34−36] For the thin films studied here, each bundle can contain up to hundreds of SWCNTs. Since $v_q \propto \sqrt{N}$,[33] the plasmon frequency is higher than would otherwise be expected for these tube lengths (over 1 μm for semiconducting tubes and around 200 nm for the metallic tubes, according to AFM).

After HgTe filling, the infrared attenuation of the semiconducting SWCNTs was found to remain almost the same, while that of the metallic SWCNTs displayed a significant reduction in strength and a substantial red-shift. These results indicate that HgTe filling did not lead to a significant change in the equilibrium charge carrier density of the semiconducting SWCNTs but can efficiently lower the free carrier density in the metallic SWCNTs. Pseudogaps have been reported to open when metallic tubes form bundles,[37] which might therefore reduce the free carrier density and conductivity of bundles of metallic SWCNTs. In this case however the pronounced difference between reference and filled metallic samples, which had similar bundle number, allows us to infer that the IR absorbance was changed by the presence of HgTe. We advance the hypotheses that the presence of HgTe NWs either modifies the band structure of each individual metallic SWCNT or alters the pseudogap derived from intertube coupling in bundles, but further work is needed to clarify the observed changes.

Excitonic Photoluminescence. The excitonic absorption and emission energies for different chirality semiconducting SWCNTs can be quantified using photoluminescence excitation (PLE) maps under S_{22} or S_{33} excitation. Following absorption, rapid relaxation to the lowest (S_{11}) excitonic state occurs before light is emitted. PLE maps of the unfilled (Figure 2(d)) and HgTe-filled (Figure 2(e)) semiconducting samples are shown, along with the transition wavelengths expected from the empirical Kataura model[32] for each (n,m) (black filled squares). The PLE map of the unfilled semiconducting sample reveals that (7,6) and (7,5) are the two most abundant (n,m) species. After HgTe filling, (8,3), (7,5), (10,2), (9,4), and (8,6) displayed a dramatic relative enhancement in their fluorescence, while the (7,6) fluorescence strength was relatively lower. PLE profiles averaged over the entire spectral window and for windows covering only particular species are shown in Figures S5 and S6. The higher fluorescence intensity from HgTe-filled semiconducting SWCNTs points toward either reduced nonradiative interactions for S_{11} excitons or a greater radiative rate. Later in the Article we turn to transient absorption spectroscopy to investigate this further.

By exciting the semiconducting samples at NIR wavelengths (850−1000 nm) close to S_{11}, additional PLE signals were resolved (Figure S7, black circles) beneath the first-order

https://doi.org/10.1021/acsnano.2c01647
ACS Nano 2022, 16, 6789−6800

Rayleigh scattering line, which can be assigned to emission at the G-mode phonon sidebands of the S_{11} excitons.[38] After HgTe NW filling the semiconducting SWCNTs presented an additional signal peak centered at ∼1060 nm (Figure S7), further evidencing stronger emission from (10,2) CNTs after filling.

In addition to changes in fluorescence intensity, small shifts in maxima were observed for specific (*n*,*m*) species: for instance the fluorescence peaks of (7,5), (9,4), and (8,6) shifted diagonally toward larger excitation and emission wavelengths. In contrast, the PLE peak for (6,5) SWCNTs (0.75 nm diameter) was not altered, suggesting that filling did not alter the energy of the excitonic states or that the narrowest tubes were not as filled.

Phonons and Electron−Phonon Coupling Assessed by Raman Spectroscopy. The anti-Stokes Raman resonances were investigated in order to confirm chirality assignments and to examine the vibrational modes and electronic properties of the HgTe-filled nanocomposites. Radial breathing modes (RBMs) of the nanotubes were observed at Raman shifts of 200−350 cm^{-1} (Figures 3(a),(b) and S8), in accord with the small (<1 nm) diameters of these SWCNTs. Under an excitation wavelength of 660 nm (an energy of 1.88 eV), two intense peaks were found at 267 and 286 cm^{-1} (Figure 3(a)) for the semiconducting SWCNTs. According to the relation $d_t = a/\omega_{RBM}$, where a = 237 nm cm^{-1} and ω_{RBM} is the wavenumber of the RBM,[39] these two RBM features correspond to d_t = 0.89 nm and d_t = 0.83 nm, *i.e.*, (7,6) and (7,5) SWCNTs, respectively. In contrast, for the metallic samples, the RBMs are reported in Figure 3(b) (488 nm excitation, close to the M_{11} absorption peaks) and in Figure S8(b1) and (b2) (under excitation at 514 and 532 nm, respectively)[40] and result from (8,5) tubes (∼266 cm^{-1}) and small fractions of (7,7) tubes (∼250 cm^{-1}).

It is noted that HgTe NW filling results in a slight softening (or red-shifting) of the RBM Raman shift for both semiconducting and metallic SWCNTs. This is somewhat unanticipated, as molecular filling normally favors the hardening (blue shifting) of the RBM, as previously demonstrated by both theoretical[41] and experimental[19,23] results. The reason behind this warrants further study.

The Raman spectra of SWCNTs at higher frequencies, such as the tangential mode (G mode) and the double resonance G′ mode, provide a further route to investigate the changes in the electronic properties of the SWCNTs induced by the HgTe zigzag filling. In the current work, five laser excitation wavelengths were applied (488, 514, 532, 633, and 660 nm, corresponding to 2.54, 2.41, 2.33, 1.96, and 1.88 eV), making it possible to uncover the resonant Raman features of different (*n*,*m*) species in semiconducting and metallic samples. Raman spectra were analyzed by subtracting a linear baseline and then fitted by a superposition of Lorentzian functions.

The Raman-active G band of SWCNTs contains multiple peaks as a result of the curvature of the SWCNT, which yields different C−C vibrational frequencies for the axial and circumferential directions.[42,43] Spectra of the G modes for the semiconducting SWCNTs under 660 and 633 nm excitation are shown in Figures 3(c) and S9(a). In both cases, the best fit to the experimental spectrum required five or six Lorentzians, which can be attributed to zone-center phonon modes with A_{1g}, E_{1g}, and E_{2g} symmetries.[44] The strongest, higher-frequency band (or G^+ band) consists of two Lorentzians centered at ∼1590 and ∼1600 cm^{-1}, which are assigned to the A_{1g}+E_{1g} and E_{2g} modes, respectively. The low-frequency band (or G^- band) comprised three Lorentzians, which can be assigned to another E_{2g} and two A+E modes. The double-resonance G′ modes are linked to two-phonon scattering processes near the K-point[45,46] and are reported in Figure 3(d) for the semiconducting SWCNTs (along with Figure S9(b)). One strong peak was observed around 2600 cm^{-1}, which was decomposed into Lorentzian peaks.

Filling with HgTe NWs red-shifted all of the G and G′ modes of the semiconducting SWCNTs, as indicated by the difference in Raman peak position after filling, $\Delta\omega$, in Figure 3(e). While the G^+ resonance position is insensitive to CNT diameter, it red-shifts when relatively more electrons are present on the CNTs,[43,47] suggesting the filling has acted like a weak donor.

The G and G′ spectra of the metallic filled and unfilled SWCNTs (Figures 3(f,g), S9(c,d), and S10(b)) are more complex than the spectra for the semiconducting samples. The so-called G^- mode of metallic tubes, covering the 1500−1550 cm^{-1} region in Figures 3(f) and S9(c), displays a distinct spectral shape that can be described by the Breit−Wigner−Fano (BWF) line shape and is thought to result from the down-shifting and broadening of the axial tangential Raman mode after strong coupling to the electronic continuum of metallic tubes.[48] While the BWF line can be clearly seen for non-armchair metallic SWCNTs, such as (8,5), it is absent in the Raman spectra of armchair SWCNTs such as (6,6) or (7,7). The asymmetric BWF line for non-armchair metallic SWCNTs can be expressed as[49]

$$I(\omega) = I_0 \frac{[1 + (\omega - \omega_{BWF})/q\Gamma]^2}{1 + [(\omega - \omega_{BWF})/\Gamma]^2} \quad (1)$$

where the parameter q describes the coupling strength between the phonon and the electronic continuum, ω_{BWF} is the wavenumber of the maximum intensity I_0, and Γ describes the line broadening. Here the BWF line at 1540−1550 cm^{-1} and a Lorentzian component at ∼1580 cm^{-1} are assigned to the non-armchair metallic species (8,5), while a narrower Lorentzian peak at ∼1590 cm^{-1} is linked to the G^+ mode of armchair species[50,51] or of residual semiconducting tubes.[48] The G′ modes of the metallic tubes (Figure 3(g)) showed a clear double-peak structure, which is only found for non-armchair metallic tubes[43] and which results from trigonal warping around the K-point.[43]

After filling with HgTe chains, the BWF feature further downshifts and broadens in width (Figure 3(f)), with a filling-induced shift $\Delta\omega \simeq -5$ cm^{-1} (Figure 3(h)). Under 488 nm excitation the spectral broadening increased from Γ = 24 cm^{-1} to 32 cm^{-1} after filling (from 21.5 cm^{-1} to 26 cm^{-1} with 514 nm excitation). A summary of the fit parameters for the BWF models is provided in Table S1. The line width of this Raman mode was previously linked to the electron−phonon coupling rate *via* electrostatically gated Raman spectroscopy on individual metallic SWCNTs.[52] We therefore deduce that the HgTe chains induce a stronger electron−phonon interaction in metallic tubes.

The intensity ratio of the disorder band (D band) to the G^+ band, a value reflecting the degree of imperfection of the sp^2 carbon lattice,[53] showed nearly no change after the HgTe filling experiment (Figure S11), indicating that any structural damage caused by the filling process is negligible. This result, in conjunction with the TEM results, provides convincing

https://doi.org/10.1021/acsnano.2c01647
ACS Nano 2022, 16, 6789−6800

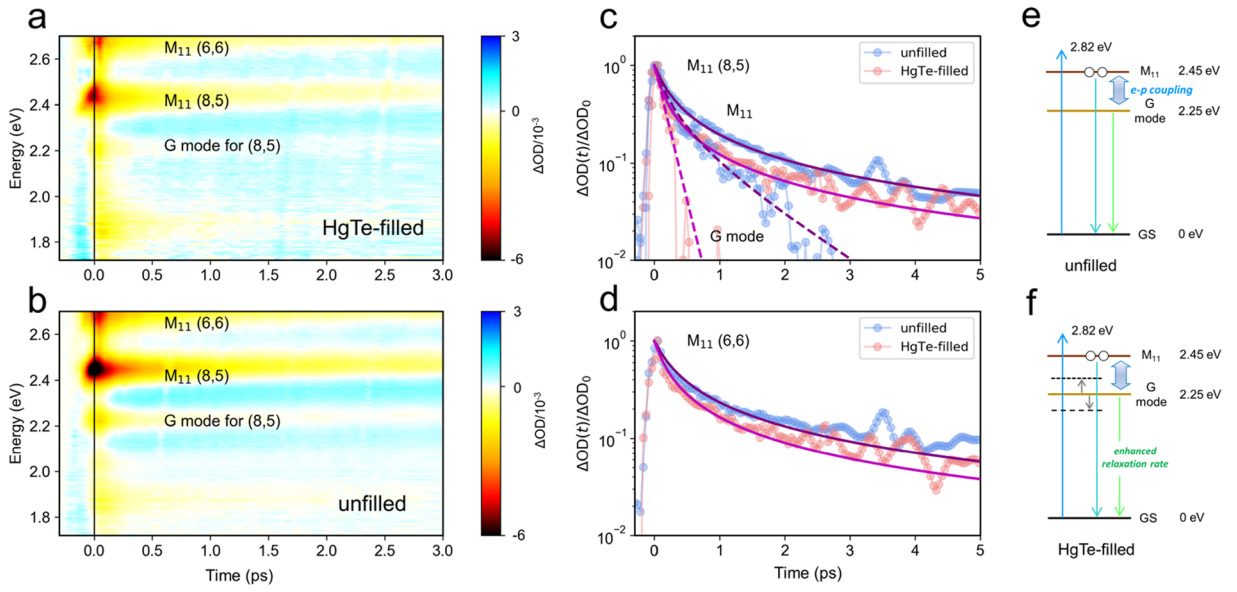

Figure 4. (a, b) Variations of the TA signals (ΔOD) against the pump−probe time delay and the probe energy for the solution-state (a) HgTe-filled and (b) unfilled metallic SWCNTs. The applied pump energy and fluence were 2.82 eV (440 nm) and 1.13 mJ cm^{-2} per pulse, respectively. (c, d) TA kinetics of the M_{11} bands for (8,5) and (6,6) as well as the G mode of (8,5). Fits (purple for the unfilled and magenta for the HgTe-filled) are as described in the text, based on the bimolecular rate equation model in eq 3. (e, f) Energy diagrams and possible relaxation pathways for (8,5) (e) without and (f) with HgTe filling. The arrow denotes electron−phonon (e−p) coupling, and the upward blue arrow marks the pump energy. The extra phonon states (dashed lines) of the infiltrated CNTs provide additional nonradiative relaxation pathways that boost the Auger rate.

proof that the evolution of the high-frequency SWCNT Raman modes was caused by HgTe NW filling, rather than as a result of damage to the SWCNTs or extraneous material.

Summary of Steady-State Optical Properties. The experimental results from optical spectroscopy indicate that the impact of HgTe zigzag NW inclusion depends on the chirality of the encapsulating SWCNTs. Raman spectra indicate that filling enhanced electron−phonon coupling in the metallic tubes, while IR absorbance demonstrated that the long-range conductivity of thin films of metallic SWCNTs was suppressed by filling. For the semiconducting tubes, HgTe NWs did not result in substantial changes in film conductivity, but did subtly shift the excitonic transition energies and did show a small amount of electron transfer from the HgTe NWs to the carbon nanotubes.

Femtosecond Transient Absorption Spectroscopy. To investigate the differing consequences of HgTe NW incorporation for metallic and semiconducting SWCNTs in more detail, we used femtosecond transient absorption (TA) spectroscopy to study dispersed tubes in solution. This allowed the dynamics of excitons on isolated metallic or semiconducting tubes to be resolved. Experimental TA signals (change in absorbance, ΔA) against the probe energy and pump−probe delay are shown in Figure 4(a) and (b) for the metallic samples. In the heat maps, several negative photobleach (PB) features can be discerned in the experimental spectral range (dark red areas), which correspond to the M_{11} excitonic states of (6,6) and (8,5) chiralities. The feature at 2.45 eV was assumed to result mainly from (8,5) rather than (7,7), which has similar M_{11} energy, by virtue of the larger RBM weighting of (8,5) (Figure 3(b)). Also evident in the TA heat maps is a PB feature at around 2.25 eV, 0.2 eV below M_{11} for (8,5), which we assign to an exciton−phonon sideband created by the G mode. The strong electron−phonon coupling in SWCNTs can create phonon sidebands that can be seen directly in the absorption spectra of SWCNTs.[54]

In Figure 4(c) and (d) the dynamics of the (8,5) and (6,6) features are reported. The observed nonexponential transient absorption dynamics were modeled by assuming that the normalized transient absorption change $\Delta OD(t)/\Delta OD_0 = n(t)/n_0$, where $n(t)$ is the population of excitons and $n_0 = n(t = 0)$, and by assuming a rate of change of $n(t)$ given by

$$\frac{dn}{dt} = -\gamma n^2 - kn \tag{2}$$

Here the first term, including the constant γ, describes bimolecular exciton recombination processes such as Auger recombination, while k tracks monomolecular decay *via* radiative and nonradiative processes. After normalization by n_0, the time evolution of the transient absorption signal for times $t > 0$ is

$$\frac{n(t)}{n_0} = \frac{k}{(k + \gamma n_0)e^{kt} - \gamma n_0} \tag{3}$$

and hence k and γn_0 are the fit parameters. We adopted this approach to fit our TA data because the maximum exciton density n_0 is hard to quantify precisely. For the M_{11} states of (8,5) and (6,6) tubes, the decay dynamics were bimolecular throughout the experimental time window, which is the case when the monomolecular rate is much smaller than the Auger recombination rate. Good agreement between model and experiment was therefore found without the need for a contribution from k (*i.e.*, $k \ll 0.1$ THz), by taking $\gamma n_0 = 4.13 \pm 0.06$ THz and 3.27 ± 0.09 THz for unfilled (8,5) and (6,6) tubes. A full list of parameters for the fitted dynamic curves at different probe energies can be found in Table S2. The experiments were conducted under the same nonresonant excitation conditions and on samples with similar absorbance.

https://doi.org/10.1021/acsnano.2c01647
ACS Nano 2022, 16, 6789−6800

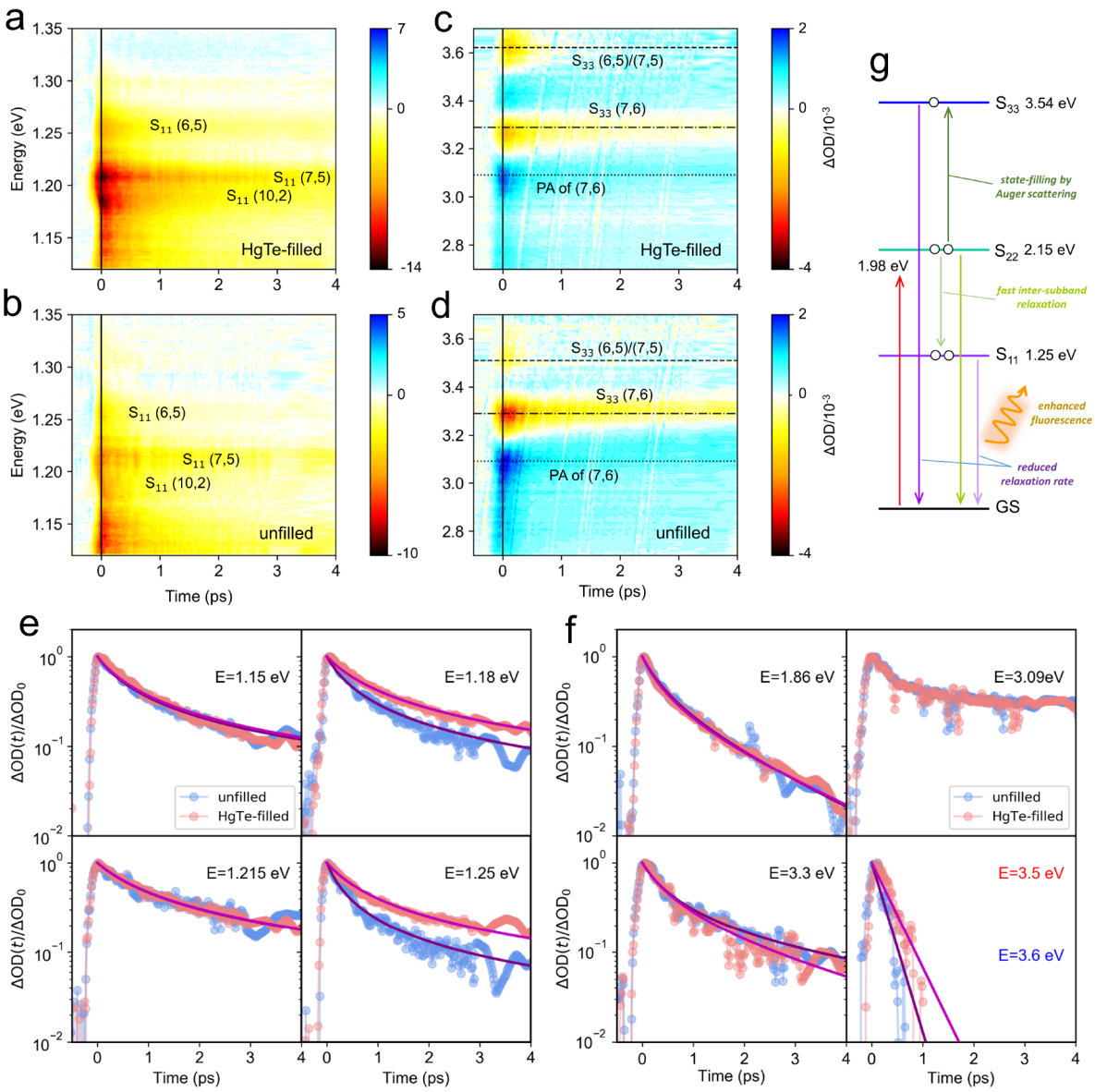

Figure 5. (a–d) Variations of the (a, b) S_{11} and (c, d) S_{33} transient absorption change (ΔOD) against pump–probe delay and probe energy for (a, c) HgTe-filled and (b, d) unfilled semiconducting SWCNTs in solution. The horizontal lines in panels (c) and (d) mark the energies of the different photobleaching (PB) and photoabsorption (PA) features. The pump photon energy and fluence were 1.98 eV (625 nm) and 1.1 mJ/cm^{-2} per pulse, respectively. (e, f) Normalized TA kinetics at different energies, (e) in the S_{11} spectral region and (f) in the S_{22} and S_{33} regions. Fits (purple for the unfilled and magenta for the HgTe-filled) are as described in the text based on the bimolecular rate equation model in eq 3). This model did not reproduce the dynamics of the PA feature at around 3.09 eV. (g) Energy diagram of (6,5) and possible exciton relaxation pathways, under the influence of HgTe NW filling, which reduced the S_{33} and S_{11} Auger rates and thus enhanced its fluorescence. The upward red arrow denotes the pump.

Assuming the same internal conversion rate to M_{11} excitons for each sample (during the first 100 fs time resolution of the pump–probe experiment), we therefore assume n_0 did not vary with chirality or filling and instead discuss the mechanisms that can alter γ.

The lower Auger rate γ for unfilled (6,6) SWCNTs in comparison to (8,5) can be understood as follows. Within a parabolic two-band approximation, *i.e.*, ignoring any electron-scattering processes between subbands and neglecting the electron–phonon interaction, the Auger rate for nanotubes can be estimated from perturbation theory to scale as $\gamma \propto (E_b/E_g)^3$, where E_b is the exciton binding energy and E_g is the single-particle energy gap.[26] The narrower diameter of (6,6) tubes (0.814 nm) increases E_g (as well as M_{11}) relative to that of (8,5) tubes (0.889 nm diameter). Hence the lower γ for (6,6) tubes may result solely from diameter-driven changes to the electronic band structure. However, this discussion ignores the important role that electron–phonon coupling plays in metallic carbon nanotubes, as evident from their Raman features (discussed above) and also evidenced by time-domain atomistic simulations of Auger decay, where two-particle exciton–exciton Auger decay processes were found to involve phonon-assisted transitions at energies up to and including the G mode.[55] Hence changes to the G mode's strength, energy, and line width may be expected to alter Auger decay rates.

https://doi.org/10.1021/acsnano.2c01647
ACS Nano 2022, 16, 6789–6800

HgTe zigzag filling directly increased the extracted Auger rates to γn_0 = 7.17 ± 0.13 THz and 5.07 ± 0.20 THz for (8,5) and (6,6) metallic SWCNTs. As there was negligible change in the M_{11} energy after filling, the around 60% higher γ for the filled tubes can be interpreted as resulting from stronger electron−phonon coupling, leading to a greater Auger rate. Further evidence for the enhanced role of electron−phonon coupling comes from the G-mode sideband (at 2.25 eV), the dynamics of which are reported in Figure 4(c). Exciton−exciton annihilation creates a single, higher energy electron−hole pair, which then relaxes by optical phonon emission. The G-sideband's dynamics for the unfilled (8,5) tubes was modeled (dashed blue line) by the same Auger term (γn_0 = 4.13 THz) but with an additional monomolecular channel at rate k = 1.0 THz, corresponding to a lifetime $\tau = 1/k$ = 1.0 ps. This is in excellent agreement with the lifetime of the G-mode phonon, τ = 1.1 ± 0.2 ps, measured directly by time-resolved Raman spectroscopy.[54] After HgTe zigzag filling, however, the G-mode sideband decayed much more rapidly and was fit (dashed red line) by a single-exponential decay with lifetime τ = 0.16 ps. This faster decay may signify that HgTe filling strains the CNTs,[17] thereby boosting the anharmonic relaxation pathways for the G-mode phonons to relax into other phonons within the SWCNT. Alternatively, the presence of encapsulated insulating nanowire chains has been shown theoretically to increase hot phonon relaxation rates by providing extra phonon decay channels.[30] The acceleration of the Auger relaxation rate in (8,5) SWCNTs due to HgTe NW filling is shown pictorially in Figure 4(e) and (f).

Finally, we investigated the impact of HgTe zigzag filling on the transient absorption spectra and dynamics for semiconducting SWCNTs in solution, under excitation at 625 nm, corresponding to the S_{22} continuum for (7,5) and (7,6) tubes. This excitation condition was adopted so as to allow the dynamics of S_{11}, S_{22}, and S_{33} excitonic absorption features to be determined, as reported in Figure 5(a) and (b) (S_{11} resonances) and Figure 5(c) and (d) (near the S_{33} resonances). After the pump pulse depopulates the second highest valence band, rapid intersubband electron scattering within 50 fs results in a reduced electron density in the highest valence band.[56] Thus, the excitonic S_{11} and S_{22} both exhibit ground-state bleaches with similar onset dynamics (<500 fs). Here we discuss the recovery dynamics.

The S_{11} spectral region was relatively congested, with ground-state bleach features associated with (10,2) SWCNTs at 1.18 eV, (7,5) at 1.21 eV, and (6,5) at 1.25 eV evident in Figure 5(a). The S_{11} energies for (7,6), (9,4), and (8,4) tubes were below the minimum energy accessible in the TA experiments (1.12 eV). Filling with HgTe chains appears to strengthen some of the ground-state bleach features, as well as slow some of the dynamics. This is evident in Figure 5(e), where transients at fixed energies are reported. At 1.15 and 1.215 eV, filling did not alter the dynamic, which could be modeled with γn_0 = 1.80 ± 0.02 THz and γn_0 = 1.13 ± 0.02 THz, respectively, ignoring k. While the dynamics at 1.215 eV corresponds to S_{11} of (7,5), the weaker TA signal at 1.15 eV (1078 nm) could result from the tail of the absorption of (10,2) or (9,4) tubes (Figure 2(e)). The TA signal at 1.18 eV becomes relatively stronger (Figure 5(a)) and slower (Figure 5(e)) after filling, and the Auger rate dropped from γn_0 = 2.37 ± 0.04 THz to γn_0 = 1.37 ± 0.01 THz with HgTe-encapsulated nanowires. A similar trend was found for (6,5), with γn_0 = 3.28 ± 0.05 THz, reducing to γn_0 = 1.50 ± 0.02 THz after filling. A lower Auger rate is consistent with an enhanced PL emission efficiency, as observed upon HgTe encapsulation for most chiralities (Figure 2(d) and (e)), since a greater fraction of excitons recombine radiatively when γ is reduced. Parameters for the fitted TA curves can be found in Table S3. An energy level diagram for HgTe-filled (6,5) SWCNTs is illustrated in Figure 5(g).

Turning to the kinetics of the higher excitonic transitions, the S_{22} resonances of (7,6) and (7,5) overlap in energy at around 1.93 eV and cannot be independently resolved. The combined S_{22} dynamics were probed at 1.86 eV, sufficiently far from the pump photon energy, and are reported in Figure 5(f) to be independent of filling. The S_{22} decay kinetics are somewhat faster than the S_{11} kinetics and were fit by a monomolecular lifetime $\tau = 1/k$ = 1.7 ps and γn_0 = 2.10 ± 0.07 THz. We interpret the bimolecular rate again as Auger two-particle recombination, while the monomolecular rate represents the time scale for S_{22} excitons to transfer to the S_{11} manifold *via* single-particle processes.

The ground-state bleach signals around 3.3 and 3.5−3.6 eV (Figure 5(c),(d)) can be assigned using the PLE results in Figure 2(d) and (e) to the (7,6) and (7,5) S_{33} resonances, respectively. The exact energies of the S_{33} and higher energy transitions have been discussed in depth in the literature,[57,58] with the consensus emerging that rather than representing transitions to bound excitonic states, S_{33} transitions can be to unbound electron−hole pairs (*i.e.*, the picture of transitions between single-particle van Hove singularities applies), as the exciton binding energy is small or negligible. Here, given the pump energy (1.98 eV) was below the energy region probed, the observed ground-state bleach absorption change can be understood as resulting from the depopulation of the ground state,[6] as well as filling the upper state *via* Auger scattering, which may promote an S_{22} exciton into an S_{33} state.[59] While the S_{33} (7,6) dynamics were not affected by HgTe encapsulation (Figure 5(f)), the transient absorption for (7,5) was blue-shifted from 3.5 eV to 3.6 eV after filling, and the decay dynamics were slowed from a monomolecular lifetime τ = 0.18 ps to 0.31 ps after filling (fit parameters are reported in Table S4). Note that the (7,5) S_{11} dynamics were not altered by filling.

These results imply that HgTe filling may alter the higher lying electronic states in a complex manner that depends on the chirality of the SWCNT. One mechanism for this is that a zigzag chain should distort the encapsulating SWCNT's cross-section into an oval,[17] modifying the electronic wave function. Moreover, a positive photoabsorption (PA) feature positioning at around 3.09 eV was discovered, with distinctly slower recombination than for the (7,5) and (7,6) S_{33} features. The dynamics at 3.09 eV were also not modified after filling with the HgTe NWs (Figure 5(f)), and the decay could not be fit well by the bimolecular model. We speculate that this PA feature may represent a transient bandgap renormalization or a change in the line width of the (7,6) S_{33} resonance.

CONCLUSION

In summary, we demonstrated experimentally that encapsulated HgTe NWs adopt a zigzag structure inside sub-1-nm-wide SWCNTs. Semiconducting SWCNTs (a few microns long) and metallic SWCNTs (less than 200 nm long) were successfully extracted from the as-prepared HgTe NW-filled raw product by a gel column chromatography method. Electron microscopic imaging revealed a dominance of zigzag

https://doi.org/10.1021/acsnano.2c01647
ACS Nano 2022, 16, 6789−6800

atomic chains in both the semiconducting and metallic SWCNTs. Steady-state optical characterization, including photoluminescence excitation spectroscopy and Raman spectroscopy, revealed that metallic and semiconducting (n,m) chiralities were altered differently by the HgTe NWs. In particular, the fluorescence of some semiconducting chiral (n,m) SWCNTs (*e.g.*, (7,5) and (9,4)) was enhanced, while that from others (*e.g.*, (7,6)) was significantly suppressed after the HgTe NW filling. The high-frequency Raman modes for the semiconducting and non-armchair (n,m) species displayed a downshifting after the HgTe filling, indicating an electron transfer from HgTe NWs to the SWCNTs and further suggested that filling enhanced electron−phonon coupling for the metallic SWCNTs. The impact of the NWs on electron−phonon and phonon−phonon coupling was investigated in the time domain *via* studies of the ultrafast transient absorption features of excitons, exciton−phonon side bands, and free carrier transitions. The faster Auger and phonon decay processes in metallic tubes after HgTe filling confirm theoretical predictions that encapsulated nanowires can modify the important functional properties of SWCNTs.

METHODS

Materials. SWCNTs produced by the CoMoCAT (ref no. 775533) were used as raw carbon nanotube products. Sodium dodecyl sulfate (SDS, ACS reagent, ≥99.0%, Sigma-Aldrich) was used as the surfactant to isolate carbon nanotubes. Mercury telluride (HgTe, 99%, Alfa Aesar) was used as the filling material. Hydrogels made from a cross-linked copolymer of allyldextran and *N,N′*-methylene bis(acrylamide) (Sephacryl S-200, GE Healthcare) were applied for the gel column chromatography experiment.

Nanowire Synthesis. Filling of SWCNTs by HgTe was conducted by melting infiltration.[12] In brief, the raw powder of SWCNTs was mechanically mixed with HgTe powder (VMR 99.999%) and then loaded into the silica quartz ampule. After being sealed under vacuum, the ampule was heated to 770 °C for 12 h followed by 670 °C for 3 h. After heating, the HgTe-filled SWCNT powder was dispersed, centrifuged, and sorted based on the methods introduced below.

SWCNT Dispersing and Sorting. The powder-like SWCNT raw material was added to an aqueous SDS solution (2 wt %) and then dispersed by a tip sonicator (150 W, 20% power output) under pulsed mode (2 s power on and 2 s power off) for at least 15 h. The catalyst particles and large nanotube bundles were removed by centrifugation at 197000*g* for 0.5 h. With this process, the sedimentation of SWCNTs was efficiently avoided.

The as-centrifuged SWCNT solutions were sorted based on a gel column chromatography approach similar to the one reported by a previous work,[60] as distinct from the pure density gradient sorting approach.[61] In brief, alkyl dextran-based gels were loaded into a glass column and equilibrated by a 2 wt % SDS solution. An SWCNT solution of about twice the volume of the gel bed was then applied to the column. After the SWCNT solution passed through the gel bed and a fraction of nanotubes were trapped, aqueous solutions containing increasing amounts of SDS (*e.g.*, 0.3, 0.5, 1.0, 1.5, 2.0, 5.0 wt %) were used to elute the nanotubes. It has been found that the fraction of semiconducting nanotubes that have the smallest diameters (*e.g.*, (6,4) and (6,5)) can be collected first. To sort nanotubes with greater diameters, pure DI water was added to the solution of SWCNTs that were not bound to the gels (to decrease the surfactant concentration to a certain value, such as 1.6 or 1.2 wt %), and the gel chromatography experiment was repeated. The outcome of diameter selection by diluting the SWCNT solution was evidenced in Figure S12, where a higher fraction of larger-diameter SWCNTs can be obtained with the concentration of SDS decreased from 2 wt % to 1.5 wt %. To extract metallic nanotubes from CoMoCAT76 SWCNTs, the as-centrifuged SWCNT solution was applied to the gel column and the first solution portion coming out from it (showing a light brown color) was collected, which had an enrichment of metallic SWCNTs.

STEM Imaging. The nanostructure of the material was determined by a doubly corrected JEOL ARM200F TEM operated under the scanning mode. The microscope was equipped with CEOS imaging aberration, probe correction and a Gatan SC1000 ORIUS camera with a 4008 × 2672 pixel CCD. Imaging was conducted under an acceleration voltage of 80 and 200 kV, both of which were verified not to cause serious damage to the carbon structure. The SWCNT samples were loaded onto the lacey TEM grid by drop-casting. The TEM grids were baked in a vacuum oven at 100−150 °C for 12 h prior to characterization in order to remove contaminants such as hydrocarbon molecules. Image analyses were carried out in the Gatan Microscopy Suite (GMS) software.

Chemical Composition Analysis. The chemical compositions of the SWCNT samples were studied by EDX characterization based on a Zeiss Gemini scanning electron microscope (SEM) equipped with a silicon drift detector. A high acceleration voltage of 20 kV and a sufficiently long working distance of 8.5 cm were applied in order to collect enough X-ray signals.

AFM Imaging. The sample height and morphology of the material was studied by a Bruker Dimension Icon atomic force microscope. Measurements were carried out under peak force tapping mode at a tapping rate of 2 kHz, with an aluminum-coated SiN cantilever (tip radius: 2−12 nm, spring constant: 40 N/m, resonant frequency: ∼70 kHz, length: ∼115 μm, width: ∼25 μm) applied as the probe. While scanning, the instrument also collects the error signal (the difference between set point amplitude value and actual amplitude value), which provides the information on interaction between the cantilever tip and sample surface. The set point force value was kept under 1 nN (0.5−1 nN) throughout the experiment. The plane fit method was used to flatten (improve the quality of) the as-obtained image.

Absorbance Spectroscopy. The equilibrium-state absorbance of SWCNT samples was characterized by a Cary60 instrument (detecting 190−1100 nm or 6.53−1.13 eV), a PerkinElmer Lambda 1050 UV−vis−NIR spectrometer (260−1300 nm or 4.77−0.95 eV), and a Bruker Vertex 70 V Fourier-transform infrared spectrometer (130−2500 cm^{-1} or 0.016−0.31 eV). Both thin-film SWCNT samples, produced by a vacuum filtration approach, and solution-state samples were examined. For UV−vis−NIR absorbance measurement on solution samples, background signals attributed to the surfactant medium were subtracted. For the mid- and far-IR measurements performed on the FTIR spectrometer, a solid-state silicon beam splitter was used.

Fluorescence Spectroscopy. The photoluminescence of SWCNT solutions was examined by a Horiba Fluorolog-3 spectrometer equipped with a xenon lamp that generated a broadband white light beam. A single-grating monochromator was applied to select the excitation wavelength. A photomultiplier tube and a liquid nitrogen-cooled InGaAs detector were used to detect the fluorescence signals in the UV−vis range (below 850 nm) and at near-infrared (850−1350 nm) wavelengths, respectively. The spectrometer corrected for variations in the lamp output (by counting excitation signals from a silicon photodiode detector) and the detector monochromator's sensitivity. Before the measurement, the SWCNT liquid dispersion was loaded into a cuvette with 1 cm path length. The fluorescence was collected in a right-angle geometry. To select the excitation light in S_{22} and S_{33} wavelengths, a 490 nm long-pass filter and a 330−660 nm band-pass filter were placed after the excitation grating slit, respectively. An NIR long-pass glass filter was placed before the emission grating slit to block Rayleigh scattered light. To characterize the phonon sidebands of the SWCNTs, measurements were carried out at excitation wavelengths between 850 and 1000 nm, which required changing the excitation grating from 1200 lines/mm to 600 lines/mm.

Raman Spectroscopy. Raman spectra were investigated using either Renishaw InVia Reflex or Horiba LabRam HR Evolution spectrometers. The LabRam spectrometer was equipped with a laser excitation of 600 or 488 nm, with both lasers providing a maximum

https://doi.org/10.1021/acsnano.2c01647
ACS Nano 2022, 16, 6789−6800

optical power of 50 mW at the sample and a 600 l/mm grating. The inVia systems were equipped with 442 nm (25 mW), 514.5 nm (38 mW), 532 nm (20 mW), and 633 nm (10 mW) with maximum powers at the sample as indicated. All data on the Invia system were collected using a 1800 l/mm grating except for the 442 nm excitation, for which a 2400 l/mm grating was used. To get a desired S/N ratio while avoiding heating or damaging the sample, the laser power was reduced to 1% to 5% of its maximum, except for the case of 442 nm excitation, for which a power output of 50% was applied to get a sufficient signal intensity. The laser beam was brought to a micron-scale spot focus (<5 μm) onto the sample by a 50× objective lens, with an NA of 0.9. Spectra were collected in the backscattering configuration. The samples for Raman measurement were prepared by a drop-casting method on a quartz substrate.

Transient Absorption Spectroscopy. The exciton dynamics of solution-state SWCNTs were examined using a TA spectrometer. Both the pump beam and the probe beam were derived from an optical parametric amplifier (TOPAS), which was seeded with a 1 kHz, 40 fs, 800 nm pulse generated by an amplified Ti:sapphire laser (Newport Spectra Physics Spitfire Ace PA). The pump beam was mechanically chopped at 500 Hz. Different white light probe continua (330−720 and 700−1100 nm) were produced from a CaF_2 crystal pumped at 800 nm and a sapphire crystal pumped at 1300 nm, respectively. A set of neutral-density filters and narrow band-pass filters were placed in the beam path to avoid saturation of the detector while affording a broadband white light supercontinuum. The pulse width/duration of the setup was 40 fs, which defined the resolution of the experiment. The acquired TA signals were chirp-corrected. For the semiconducting SWCNT samples, a pump wavelength of either 625 or 690 nm was chosen to satisfy the condition of S_{22} resonance. For the metallic SWCNT samples, a pump wavelength of 440 nm, which was slightly shorter than the M_{11} wavelengths (~460 and ~507 nm), was chosen to avoid pump scatter in the probe beam direction.

ASSOCIATED CONTENT

Supporting Information

The Supporting Information is available free of charge at https://pubs.acs.org/doi/10.1021/acsnano.2c01647.

Additional microscopy images; EDX, UV−visible, PL, and Raman spectra; fit parameters (PDF)

AUTHOR INFORMATION

Corresponding Authors

Ziyi Hu − *Department of Physics, University of Warwick, Coventry CV4 7AL, United Kingdom*; Email: ziyi.hu@warwick.ac.uk

Jeremy Sloan − *Department of Physics, University of Warwick, Coventry CV4 7AL, United Kingdom;* orcid.org/0000-0001-8612-7456; Email: j.sloan@warwick.ac.uk

James Lloyd-Hughes − *Department of Physics, University of Warwick, Coventry CV4 7AL, United Kingdom;* orcid.org/0000-0002-9680-0138; Email: j.lloyd-hughes@warwick.ac.uk

Authors

Ben Breeze − *Department of Physics, University of Warwick, Coventry CV4 7AL, United Kingdom*

Reza J. Kashtiban − *Department of Physics, University of Warwick, Coventry CV4 7AL, United Kingdom;* orcid.org/0000-0002-3871-1647

Complete contact information is available at: https://pubs.acs.org/10.1021/acsnano.2c01647

Notes

The authors declare no competing financial interest.

ACKNOWLEDGMENTS

Z.H. is indebted to the China Scholarship Council for support (201808230269). J.S. thanks the EPSRC (UK) for support under Grant EP/R019428/1. The authors acknowledge use of the Warwick Centre for Ultrafast Spectroscopy Research Technology Platform (RTP) facility, the Electron Microscopy RTP and the Spectroscopy RTP at the University of Warwick.

REFERENCES

(1) Rafailov, P. M.; Thomsen, C.; Kataura, H. Resonance and high-pressure Raman studies on carbon peapods. *Phys. Rev. B* **2003**, *68*, 193411.

(2) Bindl, D. J.; Safron, N. S.; Arnold, M. S. Dissociating Excitons Photogenerated in Semiconducting Carbon Nanotubes at Polymeric Photovoltaic Heterojunction Interfaces. *ACS Nano* **2010**, *4*, 5657−5664.

(3) Ghosh, S.; Bachilo, S. M.; Simonette, R. A.; Beckingham, K. M.; Weisman, R. B. Oxygen Doping Modifies Near-Infrared Band Gaps in Fluorescent Single-Walled Carbon Nanotubes. *Science* **2010**, *330*, 1656−1659.

(4) Burdanova, M. G.; Tsapenko, A. P.; Kharlamova, M. V.; Kauppinen, E. I.; Gorshunov, B. P.; Kono, J.; Lloyd-Hughes, J. A Review of the Terahertz Conductivity and Photoconductivity of Carbon Nanotubes and Heteronanotubes. *Advanced Optical Materials* **2021**, *9*, 2101042.

(5) Burdanova, M. G.; Kashtiban, R. J.; Zheng, Y.; Xiang, R.; Chiashi, S.; Woolley, J. M.; Staniforth, M.; Sakamoto-Rablah, E.; Xie, X.; Broome, M.; et al. Ultrafast Optoelectronic Processes in 1D Radial van der Waals Heterostructures: Carbon, Boron Nitride, and MoS2 Nanotubes with Coexisting Excitons and Highly Mobile Charges. *Nano Lett.* **2020**, *20*, 3560−3567.

(6) Burdanova, M. G.; Liu, M.; Staniforth, M.; Zheng, Y.; Xiang, R.; Chiashi, S.; Anisimov, A.; Kauppinen, E. I.; Maruyama, S.; Lloyd-Hughes, J.; et al. Intertube Excitonic Coupling in Nanotube Van der Waals Heterostructures. *Adv. Funct. Mater.* **2022**, *32*, 2104969.

(7) van Bezouw, S.; Arias, D. H.; Ihly, R.; Cambré, S.; Ferguson, A. J.; Campo, J.; Johnson, J. C.; Defillet, J.; Wenseleers, W.; Blackburn, J. L. Diameter-Dependent Optical Absorption and Excitation Energy Transfer from Encapsulated Dye Molecules toward Single-Walled Carbon Nanotubes. *ACS Nano* **2018**, *12*, 6881−6894.

(8) Medeiros, P. V. C.; Marks, S.; Wynn, J. M.; Vasylenko, A.; Ramasse, Q. M.; Quigley, D.; Sloan, J.; Morris, A. J. Single-Atom Scale Structural Selectivity in Te Nanowires Encapsulated Inside Ultra-narrow, Single-Walled Carbon Nanotubes. *ACS Nano* **2017**, *11*, 6178−6185.

(9) Qin, J. K.; Liao, P. Y.; Si, M.; Gao, S.; Qiu, G.; Jian, J.; Wang, Q.; Zhang, S. Q.; Huang, S.; Charnas, A.; et al. Raman response and transport properties of tellurium atomic chains encapsulated in nanotubes. *Nature Electronics* **2020**, *3*, 141−147.

(10) Carter, R.; Sloan, J.; Kirkland, A. I.; Meyer, R. R.; Lindan, P. J. D.; Lin, G.; Green, M. L. H.; Vlandas, A.; Hutchison, J. L.; Harding, J. Correlation of Structural and Electronic Properties in a New Low-Dimensional Form of Mercury Telluride. *Phys. Rev. Lett.* **2006**, *96*, 215501.

(11) Yashina, L. V.; Eliseev, A. A.; Kharlamova, M. V.; Volykhov, A. A.; Egorov, A. V.; Savilov, S. V.; Lukashin, A. V.; Püttner, R.; Belogorokhov, A. I. Growth and Characterization of One-Dimensional SnTe Crystals within the Single-Walled Carbon Nanotube Channels. *J. Phys. Chem. C* **2011**, *115*, 3578−3586.

(12) Spencer, J. H.; Nesbitt, J. M.; Trewhitt, H.; Kashtiban, R. J.; Bell, G.; Ivanov, V. G.; Faulques, E.; Sloan, J.; Smith, D. C. Raman Spectroscopy of Optical Transitions and Vibrational Energies of ~ 1 nm HgTe Extreme Nanowires within Single Walled Carbon Nanotubes. *ACS Nano* **2014**, *8*, 9044−9052.

(13) Vasylenko, A.; Marks, S.; Wynn, J. M.; Medeiros, P. V. C.; Ramasse, Q. M.; Morris, A. J.; Sloan, J.; Quigley, D. Electronic Structure Control of Sub-nanometer 1D SnTe via Nanostructuring

within Single-Walled Carbon Nanotubes. *ACS Nano* **2018**, *12*, 6023−6031.
(14) Nagata, M.; Shukla, S.; Nakanishi, Y.; Liu, Z.; Lin, Y.-C.; Shiga, T.; Nakamura, Y.; Koyama, T.; Kishida, H.; Inoue, T.; et al. Isolation of Single-Wired Transition-Metal Monochalcogenides by Carbon Nanotubes. *Nano Lett.* **2019**, *19*, 4845−4851.
(15) Eliseev, A. A.; Yashina, L. V.; Brzhezinskaya, M. M.; Chernysheva, M. V.; Kharlamova, M. V.; Verbitsky, N. I.; Lukashin, A. V.; Kiselev, N. A.; Kumskov, A. S.; Zakalyuhin, R. M.; et al. Structure and electronic properties of AgX (X = Cl, Br, I)-intercalated single-walled carbon nanotubes. *Carbon* **2010**, *48*, 2708−2721.
(16) Eliseev, A. A.; Yashina, L. V.; Verbitskiy, N. I.; Brzhezinskaya, M. M.; Kharlamova, M. V.; Chernysheva, M. V.; Lukashin, A. V.; Kiselev, N. A.; Kumskov, A. S.; Freitag, B.; et al. Interaction between single walled carbon nanotube and 1D crystal in CuX@SWCNT (X = Cl, Br, I) nanostructures. *Carbon* **2012**, *50*, 4021−4039.
(17) Kashtiban, R. J.; Burdanova, M. G.; Vasylenko, A.; Wynn, J.; Medeiros, P. V. C.; Ramasse, Q.; Morris, A. J.; Quigley, D.; Lloyd-Hughes, J.; Sloan, J. Linear and Helical Cesium Iodide Atomic Chains in Ultranarrow Single-Walled Carbon Nanotubes: Impact on Optical Properties. *ACS Nano* **2021**, *15*, 13389−13398.
(18) Talyzin, A. V.; Anoshkin, I. V.; Krasheninnikov, A. V.; Nieminen, R. M.; Nasibulin, A. G.; Jiang, H.; Kauppinen, E. I. Synthesis of Graphene Nanoribbons Encapsulated in Single-Walled Carbon Nanotubes. *Nano Lett.* **2011**, *11*, 4352−4356.
(19) Wenseleers, W.; Cambré, S.; Čulin, J.; Bouwen, A.; Goovaerts, E. Effect of water filling on the electronic and vibrational resonances of carbon nanotubes: Characterizing tube opening by Raman spectroscopy. *Adv. Mater.* **2007**, *19*, 2274−2278.
(20) Zhao, Y.; Song, L.; Deng, K.; Liu, Z.; Zhang, Z.; Yang, Y.; Wang, C.; Yang, H.; Jin, A.; Luo, Q.; et al. Individual Water-Filled Single-Walled Carbon Nanotubes as Hydroelectric Power Converters. *Adv. Mater.* **2008**, *20*, 1772−1776.
(21) Hart, M.; White, E. R.; Chen, J.; McGilvery, C. M.; Pickard, C. J.; Michaelides, A.; Sella, A.; Shaffer, M. S. P.; Salzmann, C. G. Encapsulation and Polymerization of White Phosphorus Inside Single-Wall Carbon Nanotubes. *Angew. Chem.* **2017**, *129*, 8256−8260.
(22) Guan, L.; Suenaga, K.; Shi, Z.; Gu, Z.; Iijima, S. Polymorphic Structures of Iodine and Their Phase Transition in Confined Nanospace. *Nano Lett.* **2007**, *7*, 1532−1535.
(23) Campo, J.; Piao, Y.; Lam, S.; Stafford, C. M.; Streit, J. K.; Simpson, J. R.; Walker, A. R. H.; Fagan, J. A. Enhancing single-wall carbon nanotube properties through controlled endohedral filling. *Nanoscale Horizons* **2016**, *1*, 317−324.
(24) Wang, F.; Dukovic, G.; Brus, L. E.; Heinz, T. F. The optical resonances in carbon nanotubes arise from excitons. *Science* **2005**, *308*, 838−841.
(25) Wang, F.; Dukovic, G.; Knoesel, E.; Brus, L. E.; Heinz, T. F. Observation of rapid Auger recombination in optically excited semiconducting carbon nanotubes. *Physical Review B - Condensed Matter and Materials Physics* **2004**, *70*, 1−4.
(26) Wang, F.; Wu, Y.; Hybertsen, M. S.; Heinz, T. F. Auger recombination of excitons in one-dimensional systems. *Phys. Rev. B* **2006**, *73*, 245424.
(27) Miyauchi, Y. Photoluminescence studies on exciton photophysics in carbon nanotubes. *Journal of Materials Chemistry C* **2013**, *1*, 6499.
(28) Amori, A. R.; Hou, Z.; Krauss, T. D. Excitons in Single-Walled Carbon Nanotubes and Their Dynamics. *Annu. Rev. Phys. Chem.* **2018**, *69*, 81−99.
(29) Lazzeri, M.; Mauri, F. Coupled dynamics of electrons and phonons in metallic nanotubes: Current saturation from hot-phonon generation. *Physical Review B - Condensed Matter and Materials Physics* **2006**, *73*, 165419.
(30) Vasylenko, A.; Wynn, J.; Medeiros, P. V.; Morris, A. J.; Sloan, J.; Quigley, D. Encapsulated nanowires: Boosting electronic transport in carbon nanotubes. *Phys. Rev. B* **2017**, *95*, 121408.
(31) Monti, M.; Jayawardena, K. D. G. I.; Butler-Caddle, E.; Bandara, R. M. I.; Woolley, J. M.; Staniforth, M.; Silva, S. R. P.; Lloyd-Hughes, J. Hot carriers in mixed Pb-Sn halide perovskite semiconductors cool slowly while retaining their electrical mobility. *Phys. Rev. B* **2020**, *102*, 245204.
(32) Weisman, R. B.; Bachilo, S. M. Dependence of optical transition energies on structure for single-walled carbon nanotubes in aqueous suspension: An empirical Kataura plot. *Nano Lett.* **2003**, *3*, 1235−1238.
(33) Nakanishi, T.; Ando, T. Optical Response of Finite-Length Carbon Nanotubes. *J. Phys. Soc. Jpn.* **2009**, *78*, 114708−114708.
(34) Shuba, M. V.; Paddubskaya, A. G.; Plyushch, A. O.; Kuzhir, P. P.; Slepyan, G. Y.; Maksimenko, S. A.; Ksenevich, V. K.; Buka, P.; Seliuta, D.; Kasalynas, I.; et al. Experimental evidence of localized plasmon resonance in composite materials containing single-wall carbon nanotubes. *Phys. Rev. B* **2012**, *85*, 165435.
(35) Zhang, Q.; Hároz, E. H.; Jin, Z.; Ren, L.; Wang, X.; Arvidson, R. S.; Lüttge, A.; Kono, J. Plasmonic nature of the terahertz conductivity peak in single-wall carbon nanotubes. *Nano Lett.* **2013**, *13*, 5991−5996.
(36) Shao, D.; Yotprayoonsak, P.; Saunajoki, V.; Ahlskog, M.; Virtanen, J.; Kangas, V.; Volodin, A.; Haesendonck, C.; Burdanova, M.; Mosley, C.; et al. Conduction properties of thin films from a water soluble carbon nanotube/hemicellulose complex. *Nanotechnology* **2018**, *29*, 145203.
(37) Delaney, P.; Choi, H. J.; Ihm, J.; Louie, S. G.; Cohen, M. L. Broken symmetry and pseudogaps in ropes of carbon nanotubes. *Nature* **1998**, *391*, 466−468.
(38) Tan, P. H.; Rozhin, A. G.; Hasan, T.; Hu, P.; Scardaci, V.; Milne, W. I.; Ferrari, A. C. Photoluminescence spectroscopy of carbon nanotube bundles: Evidence for exciton energy transfer. *Phys. Rev. Lett.* **2007**, *99*, 137402.
(39) Kuzmany, H.; Plank, W.; Hulman, M.; Kramberger, C.; Grüneis, A.; Pichler, T.; Peterlik, H.; Kataura, H.; Achiba, Y. Determination of SWCNT diameters from the Raman response of the radial breathing mode. *European Physical Journal B* **2001**, *22*, 307−320.
(40) Hároz, E. H.; Rice, W. D.; Lu, B. Y.; Ghosh, S.; Hauge, R. H.; Weisman, R. B.; Doorn, S. K.; Kono, J. Enrichment of armchair carbon nanotubes via density gradient ultracentrifugation: Raman spectroscopy evidence. *ACS Nano* **2010**, *4*, 1955−1962.
(41) Longhurst, M. J.; Quirke, N. The environmental effect on the radial breathing mode of carbon nanotubes. II. Shell model approximation for internally and externally adsorbed fluids. *J. Chem. Phys.* **2006**, *125*, 184705.
(42) Tuinstra, F.; Koenig, J. L. Raman Spectrum of Graphite. *J. Chem. Phys.* **2003**, *53*, 1126.
(43) Dresselhaus, M. S.; Dresselhaus, G.; Saito, R.; Jorio, A. Raman spectroscopy of carbon nanotubes. *Phys. Rep.* **2005**, *409*, 47−99.
(44) Jorio, A.; Dresselhaus, G.; Dresselhaus, M. S.; Souza, M.; Dantas, M. S.; Pimenta, M. A.; Rao, A. M.; Saito, R.; Liu, C.; Cheng, H. M. Polarized Raman study of single-wall semiconducting carbon nanotubes. *Phys. Rev. Lett.* **2000**, *85*, 2617−2620.
(45) Dresselhaus, M. S.; Dresselhaus, G.; Jorio, A.; Souza Filho, A. G.; Pimenta, M. A.; Saito, R. Single nanotube Raman spectroscopy. *Acc. Chem. Res.* **2002**, *35*, 1070−1078.
(46) Jorio, A.; Saito, R. Raman spectroscopy for carbon nanotube applications. *J. Appl. Phys.* **2021**, *129*, 21102.
(47) Rao, A. M.; Eklund, P. C.; Bandow, S.; Thess, A.; Smalley, R. E. Evidence for charge transfer in doped carbon nanotube bundles from Raman scattering. *Nature* **1997**, *388*, 257−259.
(48) Fouquet, M.; Telg, H.; Maultzsch, J.; Wu, Y.; Chandra, B.; Hone, J.; Heinz, T. F.; Thomsen, C. Longitudinal optical phonons in metallic and semiconducting carbon nanotubes. *Phys. Rev. Lett.* **2009**, *102*, No. 075501.
(49) Paillet, M.; Poncharal, P.; Zahab, A.; Sauvajol, J. L.; Meyer, J. C.; Roth, S. Vanishing of the Breit-Wigner-Fano component in individual single-wall carbon nanotubes. *Phys. Rev. Lett.* **2005**, *94*, 237401.
(50) Hároz, E. H.; Duque, J. G.; Barros, E. B.; Telg, H.; Simpson, J. R.; Hight Walker, A. R.; Khripin, C. Y.; Fagan, J. A.; Tu, X.; Zheng,

https://doi.org/10.1021/acsnano.2c01647
ACS Nano 2022, 16, 6789−6800

M.; et al. Asymmetric excitation profiles in the resonance Raman response of armchair carbon nanotubes. *Physical Review B - Condensed Matter and Materials Physics* **2015**, *91*, 205446.
(51) Hároz, E. H.; Duque, J. G.; Tu, X.; Zheng, M.; Hight Walker, A. R.; Hauge, R. H.; Doorn, S. K.; Kono, J. Fundamental optical processes in armchair carbon nanotubes. *Nanoscale* **2013**, *5*, 1411−1439.
(52) Wu, Y.; Maultzsch, J.; Knoesel, E.; Chandra, B.; Huang, M.; Sfeir, M. Y.; Brus, L. E.; Hone, J.; Heinz, T. F. Variable electron-phonon coupling in isolated metallic carbon nanotubes observed by Raman scattering. *Phys. Rev. Lett.* **2007**, *99*, No. 027402.
(53) McGuire, K.; Gothard, N.; Gai, P. L.; Dresselhaus, M. S.; Sumanasekera, G.; Rao, A. M. Synthesis and Raman characterization of boron-doped single-walled carbon nanotubes. *Carbon* **2005**, *43*, 219−227.
(54) Song, D.; Wang, F.; Dukovic, G.; Zheng, M.; Semke, E. D.; Brus, L. E.; Heinz, T. F. Direct measurement of the lifetime of optical phonons in single-walled carbon nanotubes. *Phys. Rev. Lett.* **2008**, *100*, 225503.
(55) Pal, S.; Casanova, D.; Prezhdo, O. V. Effect of aspect ratio on multiparticle Auger recombination in single-walled carbon nanotubes: time domain atomistic simulation. *Nano Lett.* **2018**, *18*, 58−63.
(56) Lüer, L.; Crochet, J.; Hertel, T.; Cerullo, G.; Lanzani, G. Ultrafast excitation energy transfer in small semiconducting carbon nanotube aggregates. *ACS Nano* **2010**, *4*, 4265−4273.
(57) Araujo, P. T.; Doorn, S. K.; Kilina, S.; Tretiak, S.; Einarsson, E.; Maruyama, S.; Chacham, H.; Pimenta, M. A.; Jorio, A. Third and Fourth Optical transitions in semiconducting carbon nanotubes. *Phys. Rev. Lett.* **2007**, *98*, No. 067401.
(58) Soavi, G.; Scotognella, F.; Viola, D.; Hefner, T.; Hertel, T.; Cerullo, G.; Lanzani, G. High energetic excitons in carbon nanotubes directly probe charge-carriers. *Sci. Rep.* **2015**, DOI: 10.1038/srep09681.
(59) Kanemitsu, Y. Multiple Exciton Generation and Recombination in Carbon Nanotubes and Nanocrystals. *Acc. Chem. Res.* **2013**, *46*, 1358−1366.
(60) Liu, H.; Nishide, D.; Tanaka, T.; Kataura, H. Large-scale single-chirality separation of single-wall carbon nanotubes by simple gel chromatography. *Nature Communications 2011 2:1* **2011**, *2*, 1−8.
(61) Arnold, M. S.; Green, A. A.; Hulvat, J. F.; Stupp, S. I.; Hersam, M. C. Sorting carbon nanotubes by electronic structure using density differentiation. *Nat. Nanotechnol.* **2006**, *1*, 60−65.

https://doi.org/10.1021/acsnano.2c01647
ACS Nano 2022, 16, 6789−6800